

Surface plasmon modes of finite, planar, metal-insulator-metal plasmonic waveguides

Jing Chen, Gennady A. Smolyakov, Steven R. J. Brueck and Kevin J. Malloy*

Center for High Technology Materials and Department of Electrical and Computer Engineering,
University of New Mexico, 1313 Goddard SE, Albuquerque, New Mexico 87106, USA

*Corresponding author: malloy@chtm.unm.edu

Abstract: The numerical analysis of finite planar metal-insulator-metal waveguide structures using the transfer-matrix formalism reveals both bound and leaky surface plasmon (SP) modes. The dispersion relations, propagation lengths and confinement factors of these SP modes are presented. The highest energy SP mode consists of non-radiative (bound) and radiative (leaky) portions separated by a spectral gap. The leaky regime is further divided into antenna and reactive mode regions. The antenna mode may be used for both free-space coupling and beam steering devices.

©2008 Optical Society of America

OCIS codes: (240.6680) Surface plasmons; (250.5403) Plasmonics; (240.6690) Surface waves; (230.7390) Waveguides, planar; (260.3910) Metal optics.

References and links

1. T. Goto, Y. Katagiri, H. Fukuda, H. Shinjima, Y. Nakano, I. Kobayashi, and Y. Mitsuoka, "Propagation loss measurement for surface plasmon-polariton modes at metal waveguides on semiconductor substrates," *Appl. Phys. Lett.* **84**, 852-854 (2004).
2. R. Charbonneau, N. Lahoud, G. Mattiussi, and P. Berini, "Demonstration of integrated optics elements based on long-ranging surface plasmon polaritons," *Opt. Express* **13**, 977-984 (2005), <http://www.opticsinfobase.org/abstract.cfm?URI=oe-13-3-977>.
3. J. A. Dionne, L. A. Sweatlock, and H. A. Atwater, "Plasmon slot waveguides: Towards chip-scale propagation with subwavelength-scale localization," *Phys. Rev. B* **73**, 035407 (2006).
4. R. Zia, M. D. Selker, P. B. Catrysse, and M. L. Brongersma, "Geometries and materials for subwavelength surface plasmon modes," *J. Opt. Soc. Am. A* **21**, 2442-2446 (2004).
5. P. Tournois and V. Laude, "Negative group velocities in metal-film optical waveguides," *Opt. Commun.* **137**, 41-45 (1997).
6. Y. Wang, "Wavelength selection with coupled surface plasmon waves," *Appl. Phys. Lett.* **82**, 4385-4387 (2003).
7. H. Shin, M. F. Yanik, S. Fan, R. Zia, and M. L. Brongersma, "Omnidirectional resonance in a metal-dielectric-metal geometry," *Appl. Phys. Lett.* **84**, 4421-4423 (2004).
8. J. S. Q. Liu and M. L. Brongersma, "Omnidirectional light emission via surface plasmon polaritons," *Appl. Phys. Lett.* **90**, 091116 (2007).
9. H. T. Miyazaki and Y. Kurokawa, "Squeezing visible light waves into a 3-nm-thick and 55-nm-long plasmon cavity," *Phys. Rev. Lett.* **96**, 097401 (2006).
10. Y. Kurokawa and H. T. Miyazaki, "Metal-insulator-metal plasmon nanocavities: Analysis of optical properties," *Phys. Rev. B* **75**, 035411 (2007).
11. G. Veronis and S. Fan, "Bends and splitters in metal-dielectric-metal subwavelength plasmonic waveguides," *Appl. Phys. Lett.* **87**, 131102 (2005).
12. F. Villa, T. Lopez-Rios, and L. E. Regalado, "Electromagnetic modes in metal-insulator-metal structures," *Phys. Rev. B* **63**, 165103 (2001).
13. E. N. Economou, "Surface plasmons in thin films," *Phys. Rev.* **182**, 539-554 (1969).
14. M. A. Gilmore and B. L. Johnson, *J. Appl. Phys.* **93**, 4497 (2003).
15. J. A. Dionne, L. A. Sweatlock, H. A. Atwater, and A. Polman, "Planar metal plasmon waveguides: frequency-dependent dispersion, propagation, localization, and loss beyond the free electron model," *Phys. Rev. B* **72**, 075405 (2005).
16. J. Chilwell and I. Hodgkinson, "Thin-films field-transfer matrix theory of planar multilayer waveguides and reflection from prism-loaded waveguides," *J. Opt. Soc. Am. A* **1**, 742-753 (1984).

17. J. J. Burke and G. I. Stegeman, "Surface-polariton-like waves guided by thin, lossy metal films," *Phys. Rev. B* **33**, 5186-5201 (1986).
 18. A. D. Rakić, A. B. Djurišić, J. M. Elazar, and M. L. Majewski, "Optical properties of metallic films for vertical-cavity optoelectronic devices," *Appl. Opt.*, **37**, 5271-5283 (1998).
 19. G. W. Hanson and A. B. Yakovlev, "Investigation of mode interaction on planar dielectric waveguides with loss and gain," *Radio Sci.*, **34**, 1349-1359 (1999).
 20. P. Berini, "Plasmon-polariton waves guided by thin lossy metal films of finite width: bound modes of asymmetric structures," *Phys. Rev. B* **63**, 125417 (2001).
 21. Y. D. Lin and J. W. Sheen, "Mode distinction and radiation-efficiency analysis of planar leaky-wave line source," *IEEE Trans. Microwave Theory Tech.* **45**, 1672-1680 (1997).
-

1. Introduction

Surface plasmons (SPs), the transverse magnetic (TM) waves propagating along metal-dielectric interfaces with fields exponentially decaying in both media, have been extensively investigated for decades. This surface localization, confining the optical mode to subwavelength scale and minimizing the optical mode size, makes plasmonic waveguides an intriguing alternative to conventional dielectric-based waveguides. Long-range SP waveguides based on thin metal films or stripes (referred to as insulator-metal-insulator (IMI) waveguides) have been studied previously [1,2], but metal-insulator-metal (MIM) SP waveguides offer higher confinement factors and closer spacing to adjacent waveguides or structures[3,4] and have been proposed for this and other potential applications [5-8]. Optical resonators based on finite-length MIM structures, called "nanosheet plasmon cavities," have been thoroughly studied [9,10]. Another study suggests that waveguide bends and splitters based on MIM subwavelength plasmonic waveguides have low loss over a wide frequency range [11].

However, previous studies on MIM structures examined either the MIM gap mode in the presence of semi-infinite metal half-spaces [3], a subset of the modes of the finite MIM structure [4,12] or dealt with full dispersion relation for multiple-film geometries only under the assumption of free-electron metals [13,14]. For completeness, we use an empirical fit of the metal dielectric function to experimental data. This results in one notable difference compared to use of a free-electron model; instead of asymptotically approaching resonance frequencies, the dispersion curves cross and form quasibound (QB) modes [15]. These are shown in Fig. 1 but will not be discussed further in this paper.

Four SP modes exist for the finite thickness MIM structure due to splitting of the coupled plasmon modes for two interacting thin metal films. The complete SP mode set for finite planar MIM waveguides with real metals is investigated for the first time in this paper, revealing both bound and leaky modes. For the leaky mode, a spectral gap forms at the light line and the mode becomes an "antenna" mode in the radiation region. This antenna mode allows angle-dependent free-space interaction with plasmonic devices and suggests steerable input and output coupling functions. The trade-offs posed by propagation lengths and confinement factors and their optimization for three bound SP modes are also described.

Due to the nature of SP modes excited on planar metal-insulator structures, only TM modes are discussed in this paper. The TM polarized SP mode is uniquely characterized by its magnetic field lying in the plane of the metal-insulator surface and perpendicular to the wave propagation direction. The modal symmetry properties (either symmetric-S or antisymmetric-A) used to label the modes in this paper are therefore defined by the symmetry of the tangential magnetic field with respect to the waveguide median plane. This description differs from other literature definitions usually based on the tangential electric field in propagation direction. The TM modal solutions of the planar MIM geometry are obtained numerically by using the standard transfer matrix formalism with a Newton-Raphson root searching algorithm in the complex wave-vector plane. This implementation has been validated to an accuracy of

10^{-9} against previously published results for lossless and lossy bound and leaky waveguides as well as plasmonic waveguides [3,16,17].

2. Dispersion and field profiles

The symmetric MIM Ag/air/Ag waveguide embedded in free space was numerically analyzed. The waveguide is centered at $x=0$ with the x -axis normal to the interfaces and wave propagation is in the positive z direction. The dielectric constant of silver is fit to experimental data over a wide spectral range (0.1 to 6 eV) by a Lorentz–Drude model, explicitly including both the intraband Drude free-electron effects and interband Lorentz bound-electron effects [18]. The wavelength range showing anomalous dispersion behavior, where $K(\omega)$ decreases with increasing frequency, will not be covered in this paper. The real part of longitudinal propagation constants, $\text{Re}\{K_z\}$, and field profiles of supported modes in MIM structure with insulator air core thickness $d_I = 300\text{nm}$ and Ag metal thickness $d_M = 50\text{nm}$ are illustrated in Fig. 1. The corresponding modal loss (imaginary part of the propagation constant) and propagation length will be discussed in Section 3.

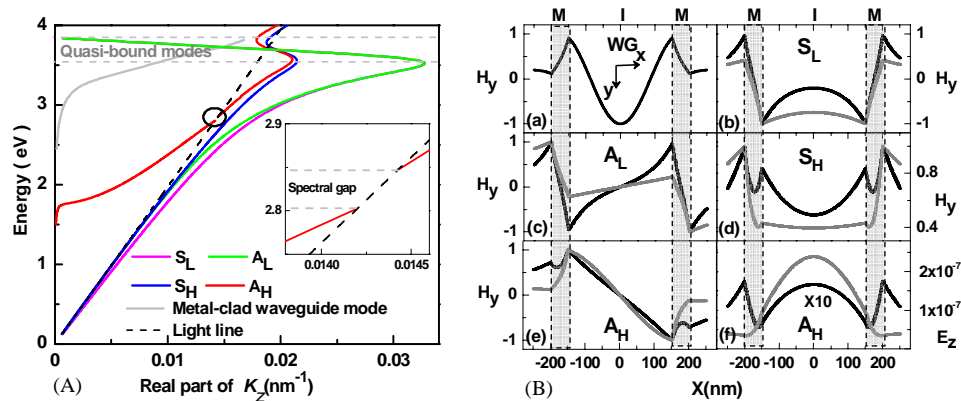


Fig. 1. TM dispersion relations (a) and characteristic tangential field profiles (B) for a symmetric Ag/air/Ag planar MIM structure bounded by free space with insulator thickness $d_I=300\text{ nm}$ and metal thickness $d_M=50\text{ nm}$. (b) illustrates fields at vacuum wavelengths of 400 nm (black) and 600 nm (gray). Panels (a)–(e) plot the tangential magnetic field (H_y) for the conventional metal-clad waveguide mode, and modes S_L , A_L , S_H , and A_H respectively. Panel (f) shows the tangential electric fields (E_z) of mode A_H .

The dispersion relation for thin metal film surface plasmons has a symmetric (S) high-energy (H) branch and an anti-symmetric (A) low-energy (L) branch. When two identical metal films interact in the MIM structure, the thin metal film SP modes undergo mode splitting, lifting their degeneracy. Therefore, two mode pairs giving a total of four non-degenerate SP modes should be observed for two interacting metal films separated by a thin insulator layer.

As shown in Fig. 1(a), quasi-bound (QB) modes [15] exist between 3.55–3.84eV and above that the radiative-coupled plasmon modes are observed. The QB modes originate from deviations in the metal from free-electron dielectric functions and will not be discussed further. Along with conventional metal-clad waveguide mode(s) at higher frequencies, four SP modes are observed for MIM structures, and are labeled S_L , A_L , S_H and A_H according to their field profiles shown in panels (b)–(e) in Fig. 1(b). Labels S/A denote the symmetric/anti-symmetric field distribution and subscript letter L/H associate the mode as originating from the low/high energy branch of the single metal film SPs.

The first conventional metal-clad waveguide mode (solid light gray in Fig. 1(a)) only exists above a cut-off energy around 2.45eV ($\sim 500\text{ nm}$), where the photon wavelength is

shorter than the round-trip optical path inside MIM structure. In each SP mode pair, the symmetric mode always has lower energy comparing to the antisymmetric mode with the same wave vector. The three lowest energy modes (S_L , A_L and S_H) always lie to the right side of the light line and remain nonradiative (bound) SP modes throughout the whole wavelength range below 3.55eV . The highest energy mode A_H is of particular interest since its dispersion relation crosses the light line and a significant portion at longer wavelengths lies above the free space light line, which normally separates nonradiative (bound) and radiative (leaky) regions. Consequently, the MIM waveguide will interact with free space without prism and grating via A_H mode leaky waves. Detailed properties of the A_H mode leaky wave as well as the spectral gap [19] (Fig. 1(a) inset) that exists between the bound and leaky regions will be presented in Section 4.

The magnitude of the fields inside the insulator is of interest for possible nonlinear applications of MIM SP waveguides. It is observed that the lowest (S_L) and highest (A_H) energy mode both have field maxima associated with the largest amount of charge located on the *internal* interface pair while in contrast, the A_L and S_H modes have the most charge localized on the two *external* interfaces. Furthermore, panel (f) of Fig. 1(b) shows the peak localization of the E_z longitudinal electric field component associated with the collective electron oscillations transitioning from the external interfaces to the insulator as the A_H mode transitions from bound to leaky. For all modes, field amplitudes inside the metal films exponentially decay away from interfacial maximums, with more rapid decay in metal field values occurring at longer wavelengths owing to shorter skin depths. Consequently, the field strength inside the insulator decreases with increasing wavelength for the A_L and S_H modes where the field peaks are localized on the external metal-insulator interfaces.

The transverse electric field E_x inside the insulator is of particular interest if nonlinear optical effects are to occur in the MIM waveguide. E_x is given by $K_z H_y$ and the surface charge at the metal surfaces has the following symmetry properties. For the low-frequency mode pair S_L and A_L , the individual metal films have the same signed charge on their inner and outer interfaces while the high-frequency mode pair S_H and A_H have oppositely signed charges. The symmetric mode pair S_L and S_H have oppositely signed charges on their internal interfaces while for modes A_L and A_H , the reverse occurs. The largest amount of oppositely signed charge on the internal interfaces and hence the largest internal insulator fields, occurs for mode S_L , making it the best candidate for nonlinear applications.

Figure 2 shows the dispersion behavior for MIM structures as a function of insulator thickness (Fig. 2(a)) and metal film thickness (Fig. 2(b)). The separation between the symmetric and antisymmetric modes for both the low energy and high energy mode pair increases with decreasing spacing between the two metal films. The S_H and S_L modes flatten away from the limiting IMI S_H and A_L modes, respectively as the insulator thickness is reduced, in contrast to the stiffening of the A_L mode. As the metal thickness decreases, the S_L and A_L modes flatten away from the limiting case semi-infinite MIM S_L and A_H modes, respectively, while the S_H mode stiffens with respect to the limiting case semi-infinite MIM S_L mode. The A_H mode exhibits more complicated variation with metal and insulator thickness that depends on considering the bound and leaky regions. The spectral gap decreases with increasing metal and insulator thicknesses. The leaky regions move to lower energy with increasing insulator thickness.

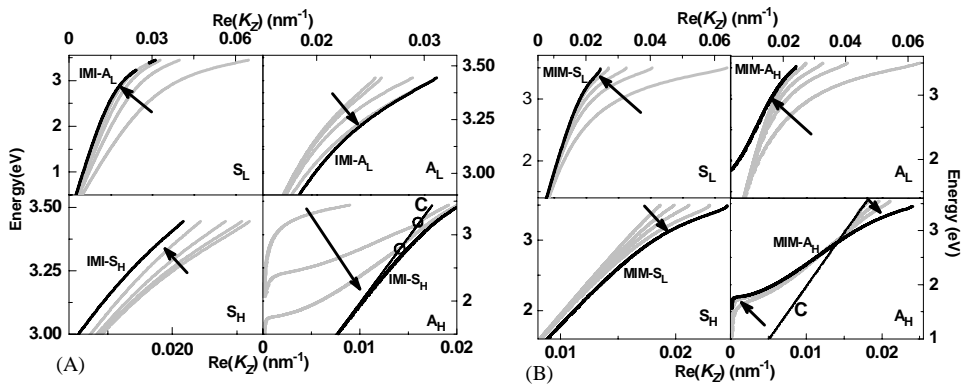


Fig. 2. MIM dispersion as a function of insulator thickness (a) and metal film thickness (b). The arrow indicates increasing thickness. The y-axis ranges of above panels are various. (a): MIM geometry with metal thickness $d_M = 50$ nm and insulator thickness $d_i = 20, 50, 100$ and 200 nm (for modes S_L, A_L and S_H) and $d_i = 100, 200$ and 300 nm (for mode A_H). Dispersion relations for air/Ag (50 nm)/air IMI waveguide, low energy antisymmetric modes (top two panels) and high energy symmetric modes (bottom two panels), are plotted in solid black lines as reference. (b): MIM geometry with insulator thickness $d_i = 300$ nm and metal thickness $d_M = 20, 35,$ and 50 nm. Dispersion relations for semi-infinite MIM waveguide, low energy symmetric modes (left two panels) and high energy antisymmetric modes (right two panels) are also plotted in solid black lines as reference.

3. Propagation length and confinement factor

The propagation length L , and the confinement factor Γ are two important parameters describing waveguide performance. The propagation length is governed by the modal loss and is defined as the distance where the traveling wave power magnitude decays by $1/e$. It is given by $L = 1/2\text{Im}\{K_z\}$, where K_z is the longitudinal propagation constant. Following the definition of confinement factor in dielectric waveguides, the confinement factor Γ represents the ratio of power propagating in the central insulator layer to the total power in the MIM waveguide [20] and is defined as follows:

$$\Gamma = \frac{\int_{\text{Insulator Layer}} \text{Re}(\vec{E}_x \times \vec{H}_y^*) dx}{\int_{-\infty}^{\infty} \text{Re}(\vec{E}_x \times \vec{H}_y^*) dx}$$

The wavelength-dependent propagation length and confinement factor of the MIM waveguide SP modes plotted in Fig. 1 are shown in Fig. 3. For the bound modes, longer propagation lengths occur at longer wavelengths where the dispersion is close to linear. Mode S_H possesses the longest and mode S_L the shortest propagation length. The long propagation length of modes A_L and S_H come at the expense of a low confinement factor. For modes A_L and S_H , the confinement factor decreases at longer wavelengths in contrast to mode S_L . Figure 1(B) shows the reason for this as at longer wavelengths, the fields of these two modes are localized on external interfaces and exponentially decay more rapidly inside the metal film owing to shorter skin depths, giving lower modal loss but also smaller fields inside the insulator. Since the confinement factors for the A_L and S_H modes are so low, the S_L mode, with both moderate propagation lengths and large confinement factors, becomes attractive for applications at long wavelength. Not shown in Fig. 3 are the characteristics of the 1st dielectric-core, metallic-cladding waveguide mode with relatively lower modal loss than the S_L/A_L SP mode pair but with a high-energy mode cut-off and high modal dispersion.

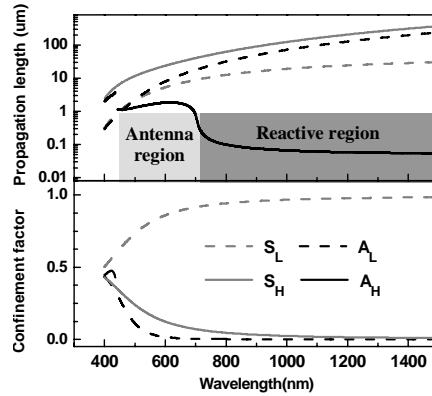


Fig. 3. Wavelength-dependent propagation length and confinement factor for a MIM structure of $d_I = 300$ nm and $d_M = 50$ nm. It is the same waveguide structure as that in Fig. 1.

For mode A_H , the leaky portion has a shorter propagation length compared to any of the bound modes due to radiation loss and the material losses inside the metal. Upon closer scrutiny, the sharp decrease in propagation length occurring around 700 nm, is a transition from the shorter wavelength, antenna region to the longer wavelength, reactive region, and will be discussed in Section 4.

The behaviors of L and Γ in MIM plasmonic waveguides as a function of metal and insulator thickness are summarized in Fig. 4. Thicker metal/insulator layers favor the S_L/S_H modes, respectively, with longer propagation distances as well as higher confinement factors. Maximum sub-wavelength confinement, far beyond that achievable in an IMI structure, is obtained in mode S_L at the cost of moderately higher loss. Mode S_H is characterized by longer propagation distances but only moderate confinement factors. It is also observed that the L and Γ of the MIM configuration asymptotically approaches that of the limiting IMI/semi-infinite MIM structure with increasing insulator/ metal thickness, respectively, as expected.

Compared with the A_L and S_L mode pair, the S_H mode deviates from IMI characteristics over a larger range of insulator thicknesses. This reflects the fact that in the IMI high-energy mode branch, the SP field penetrates further into the adjacent dielectric. Waveguide mode A_L has extremely small confinement factors for MIM structures with metals thicker than about 50 nm and hence is probably not suitable in any application requiring confinement.

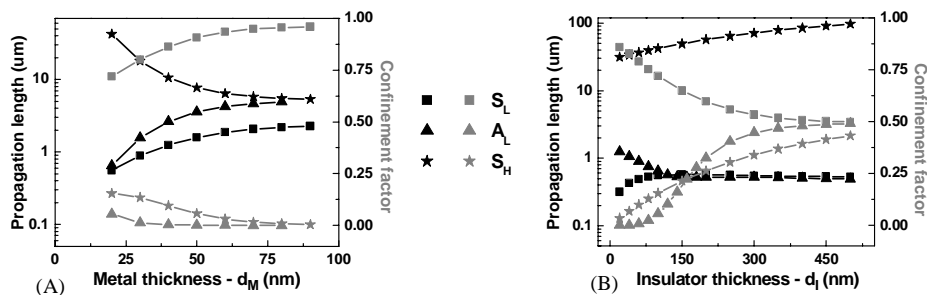


Fig. 4. Propagation length L (black lines and symbols) and confinement factor Γ (gray lines and symbols) for the MIM plasmonic waveguide at a free-space wavelength of 500 nm as a function of (A) metal (B) insulator) thickness with fixed (A) insulator thickness $d_I = 100$ nm (B) metal thickness, $d_M = 20$ nm.

4. Leaky wave analysis

Leaky modes, possessing exponentially increasing fields (referred to as *improper* field profiles) in one or both of the bounding media (as opposed to bound modes with exponentially decaying *proper* field profiles away from the structure), are mathematically valid but “improper” solutions of the same eigenvalue problem used to find the guided modes. The modes character changes between *proper* and *improper* to make every “mode” analytically continuous in the complex frequency plane with every other “mode” [19]. Whether a *proper/improper* solution is physically real is determined by the requirement that the real part of mode effective index be greater/less than the index of outmost bounding media. This results in spectral gaps in the dispersion curve when a mode changes from bound to leaky upon crossing the light line.

The MIM A_H mode crosses the light line, thus changing in character from bound mode to leaky mode. The transition at the light line is characterized by a spectral gap, while in the leaky region, the A_H mode can be divided into an antenna mode region and a reactive mode region [21]. The spectral gap occurs because mathematically there are two eigenvalues for the A_H mode: a bound mode (proper solution) that becomes unphysical above the light line because the modal index is less than the outermost media index, and a leaky mode (improper solution) that becomes unphysical below the light line because the modal index is greater than that of the outermost media.

Above the light line, the mode is a physically leaky mode composed of two distinct regions: an antenna mode region defined by $\text{Re}\{K_z\} > \text{Im}\{K_z\}$, and characterized by the propagation of mode energy out of the waveguide, and a reactive mode region defined by $\text{Re}\{K_z\} < \text{Im}\{K_z\}$ [21]. This causes the imaginary part of the transverse wave vector to increase, but because the propagation constant is predominantly imaginary, radiation loss is limited.

This leaky mode behavior results in a wave-front tilt, θ , away from parallel to the MIM structure. Following the analysis of radiative modes in thin metal films presented in Ref. [17], the wave-front tilt is defined as $\tan(\theta) = \text{Im}\{K_x\} / \text{Re}\{K_z\} = \text{Im}\{K_z\} / \text{Re}\{K_x\}$, where $K_x = (K_z^2 - k_0^2)^{1/2}$, k_0 is the free space wavenumber and K_x is the complex transverse propagation constant in the outermost media.

To find the radiated power, the exponentially increasing local field is replaced by an effective appropriately phased equivalent current sheet [17]. The angular dependence of the radiated power is expressed as:

$$|P(\theta)|^2 = \frac{\sin^2(\theta)}{(\text{Re}\{K_z\} - k_0 \cos(\theta))^2 + (\text{Im}\{K_z\})^2}$$

For this mode, there is a well-defined peak in $|P(\theta)|^2$ at $\theta = \cos^{-1}(\text{Re}\{K_z\}/k_0)$, with an angular spread proportional to $\text{Im}\{K_z\}$. The actual radiation pattern as a function of insulator and metal thickness are plotted in Fig. 5(B).

As shown in Fig. 5(A), the radiation angle increases with increasing wavelength until becoming perpendicular to the waveguide interface. The antenna region, always at shorter wavelengths relative to the reactive region, shifts to longer wavelength with smaller peak radiation tilt as insulator thickness increases. Both the insulator and metal thickness have an influence on the antenna mode’s well-defined radiation pattern, but practical considerations might lead to better control over the radiation pattern with varying insulator thickness. Narrower radiation lobes are found for thicker metal films. This variation of radiation angle with wavelength and insulator thickness can be understood in terms of the real part of the propagation constant ($\text{Re}\{K_z\}$) and the imaginary part of the transverse wave vector ($\text{Im}\{K_x\}$) in the free space regions bounding the waveguide. Increasing wavelength and decreasing insulator thickness both result in a decrease in $\text{Re}\{K_z\}$, implying an increase of $\text{Im}\{K_x\}$ and leading to an increase in radiation angle.

Numerical modeling of one-sided Au/SiO₂/Au (30 nm/190 nm/semi-infinite) MIM leaky structures shows the presence of the antenna mode in the near-infrared at about 750 to 825 nm.

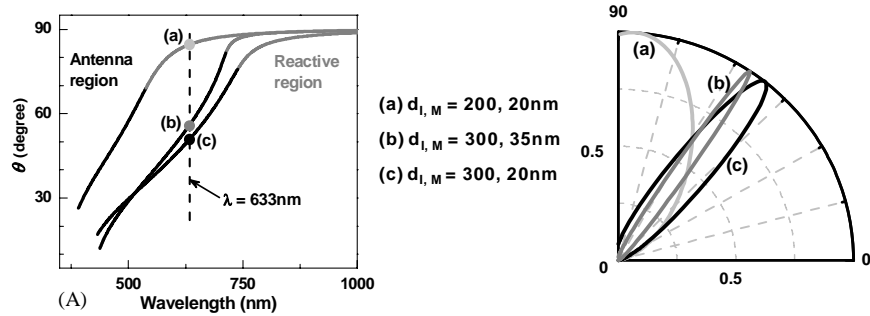


Fig. 5. MIM leaky wave-front tilt θ (A) and radiation free-space coupling pattern at a free-space wavelength of 633nm (B) as a function of insulator and metal thickness ($d_{I,M}$). In (A), the transition from black to gray in the plot curves occurs at the wavelength where the MIM waveguide modal propagation constant has equal real and imaginary values.

5. Conclusions

Analysis of the complete surface plasmon mode set dispersion relations for a finite planar MIM structure with empirical Drude-Lorentz metal parameters has been presented in this paper. The plasmon mode structure is found to consist of three complete bound modes and one higher energy mode that has bound and leaky regions separated by a spectral gap at the light line. The leaky region is further divide into a reactive region and an antenna region. This MIM waveguide antenna mode is a means of angle-dependent free-space coupling to plasmonic devices and might be useful for steerable input and output coupling functions.

Acknowledgment

This work was supported by DARPA OMC University Photonics Research Center.